Research Article

# Achieving Remarkable Amplification of Energy-Storage Density in Two-Step Sintered NaNbO₃−SrTiO₃ Antiferroelectric Capacitors through Dual Adjustment of Local Heterogeneity and Grain Scale

Aiwen Xie, He Qi, and Ruzhong Zuo*

ACCESS | Metrics & More | Article Recommendations

**ABSTRACT:** Antiferroelectric (AFE) materials exhibit outstanding advantages against linear or ferroelectric (FE) dielectrics in high-performance energy-storage capacitors. However, their energy-storage performances are usually restricted by both extremely large hysteresis and insufficiently high driving field of the AFE-FE phase transition, which has been a longstanding issue to be overcome in the community. In this work, we report a two-step sintered $0.83NaNbO_3$-$0.17SrTiO_3$ (NN-ST) lead-free relaxor AFE R-phase ceramic with high relative density of ≥95% and large spans of average grain sizes from 1.2 to 8.2 $\mu$m, strikingly achieving a giant amplification of recoverable energy-storage density ($W_{rec}$) by 176%. Analyses of permittivity-temperature curves, Raman spectrum and micro-structure demonstrate that remarkably enhanced $W_{rec}$ values should be ascribed to the dual adjustment of local heterogeneity (nanoscale) and grain scale (microscale), resulting in the enhanced threshold field strength for dielectric breakdown and the increased critical electric fields for the AFE-FE phase transition. A high $W_{rec} \approx 1.60$ J/cm³, a fast discharging rate $t_{0.9} \approx 520$ ns, large current density ~788 A/cm², and large power density ~55 MW/cm³ are achieved at room temperature in the NN-ST ceramic sample with an average grain size of ~1.2 $\mu$m. These results suggest that the multiscale structure regulation should be an efficient way for achieving enhanced energy-storage properties in NN-ST relaxor AFE ceramics through a two-step sintering technique.

**KEYWORDS:** lead-free, relaxor antiferroelectric, energy storage, NaNbO₃, two-step sintering
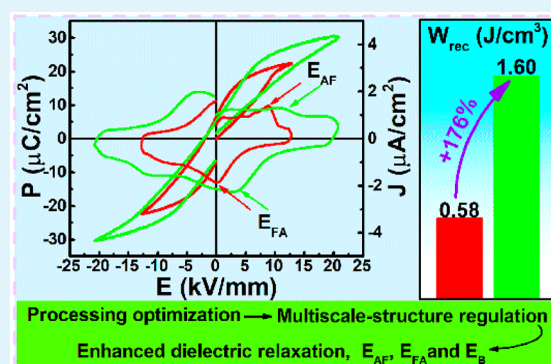
## 1. INTRODUCTION

Antiferroelectric (AFE) materials exhibit unique double polarization versus electric field ($P-E$) hysteresis loops as a result of electric field induced reversible AFE-ferroelectric (FE) phase transition, clearly showing large advantages in energy-storage capacitors because of relatively large polarization difference $\Delta P$ (= $P_{max} - P_r$, where $P_{max}$ is maximum polarization and $P_r$ is remanent polarization), compared with linear dielectrics or FEs.[1−5] It has been found that the adjustment of the critical electric fields for phase transition and the improvement of the breakdown strength ($E_B$) should be crucial for realizing excellent energy storage properties of an AFE ceramic.[6−9] Giant recoverable energy-storage density ($W_{rec}$) of 3−11 J/cm³ was reported in PbZrO₃-based AFE ceramics.[8−11] However, considering the detrimental effect of lead oxide on the environment and human health, more and more attention has been paid to lead-free AFE ceramics in recent years.[12−17]

Because of the existence of multiple AFE phases with changing temperature, NaNbO₃ (NN)-based ceramics have attracted a lot of interests for energy-storage capaci-tors.[7,13,14,18,19] Pure NN ceramic exhibits an AFE ortho-rhombic P phase (*Pbma* space group) at room temperature and transforms into an AFE orthorhombic R phase (*Pnma* space group) at about 360 °C on heating.[20] However, because of the electric-field-induced irreversible AFE to FE phase transition,[21,22] pure NN ceramics should display poor energy-storage properties at room temperature, as shown in Figure 1a. Recent studies demonstrated that repeatable double $P-E$ loops can be obtained in both P[21,23] and R[7] phase after the addition of some ABO₃ perovskites, which should increase the application potentials of NN-based AFEs in energy-storage capacitors. For example, CaZrO₃ was reported to stabilize the AFE P phase with improved $W_{rec}$ of ~0.55 J/cm³ and $\eta$ of
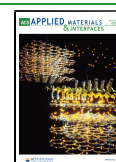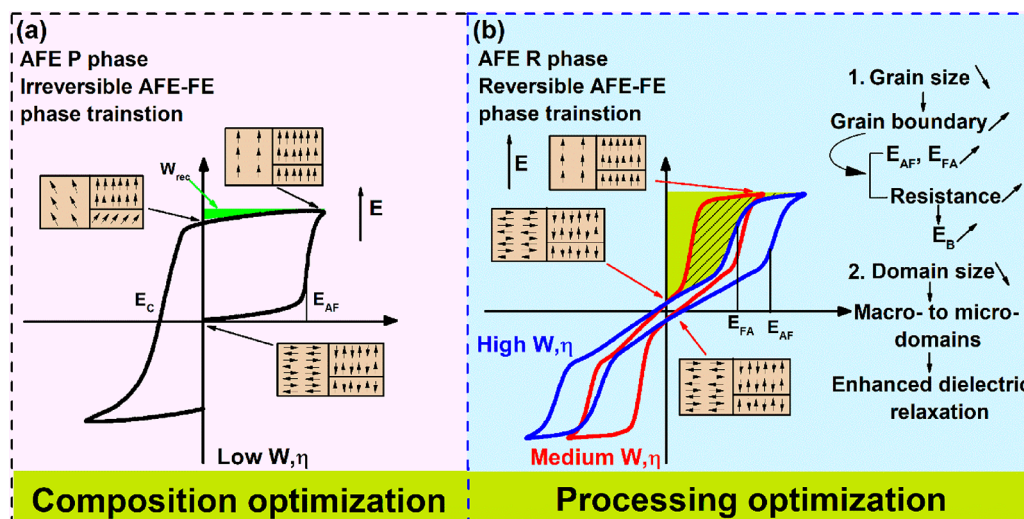
**Figure 1.** Schematic diagram of $W_{rec}$ in NN-based AFE (a) P-phase and (b) R-phase ceramics by means of composition and processing optimization.

63%,[22] whereas $(Bi_{0.5}Na_{0.5})TiO_3$ was reported to induce the AFE R phase at room temperature with high energy-storage performances ($W_{rec}$ of ~12.2 J/cm³ and $\eta$ of 69%).[7] Compared with the AFE P phase, the AFE R-phase NN-based ceramics have relatively low-hysteresis $P-E$ loops,[7] meaning relatively large potentials in energy-storage properties. In addition to the composition design, the effect of processing optimization on the energy-storage performance of NN-based AFE ceramics has been rarely investigated until now.

Besides the perovskite additives, the phase stability of AFE ceramics can also be affected by processing,[24-26] as indicated in Figure 1b. On the one hand, the reduction of grain size tends to enhance the stability of the AFE phase, thus affecting the critical electric field for AFE-FE ($E_{AF}$) and FE-AFE ($E_{FA}$) phase transition.[26,27] Furthermore, the change of grain size proves to be closely related with the $E_B$ value, generally showing a reciprocal relation between them.[28,29] This should be basically ascribed to the high resistivity of grain boundary.[30] As a consequence, changing sintering atmosphere,[31] introducing dopants[27] and adopting some special sintering methods (including spark plasma sintering,[32,33] microwave sintering,[34,35] liquid phase sintering,[36,37] and two-step sintering[29,38] have been used to densify the ceramic body simultaneously with desirable microstructure. On the other hand, the processing of the ceramic also exhibits an obvious influence on dielectric properties, particularly inducing obvious dielectric relaxation behavior.[39-41] Because of the local composition inhomogeneity, which induces the formation of random (electric or strain) fields, the appearance of relaxor characteristics in FE or AFE ceramics proves to be efficient in adjusting domain switching, phase transition, and energy-storage properties.[7,42-45]

The $(1-x)$NN-$x$SrTiO₃ ($(1-x)$NN-$x$ST) binary system has been systematically investigated in terms of local and average structure evolutions, and exhibits an AFE orthorhombic R phase at room temperature at $x > 0.14$ and excellent energy-storage properties at $x = 0.20$ ($W_{rec} \approx 3.02$ J/cm³ @ 31 kV/mm).[46,47] Repeatable slim and double $P-E$ loops as well as large polarization difference make NN-ST R-phase ceramics a competitive lead-free AFE candidate for energy-storage application. However, $E_{AF}$ is not high enough compared with

some other NN-based AFEs and the $E_B$ also needs to be improved. In this work, the 0.83NN-0.17ST AFE ceramic was chosen as a case composition and densified by a two-step sintering method to demonstrate how the energy-storage properties can be correlated with the adjustment of microstructure of different scales. A series of well-dense AFE ceramic samples with large spans of average grain size were obtained by varying sintering parameters, aiming at exploring their energy-storage characteristics and relevant physical mechanisms. The results demonstrate a giant amplification by 176% of the energy-storage density $W_{rec}$ in the processing modulated AFE ceramic, which was attributed to the dual adjustment of local inhomogeneity and grain scale by means of dielectric permittivity versus temperature and frequency spectra, Raman spectra, and quantitative analysis of grain size.

## 2. EXPERIMENTAL SECTION

The 0.83NN-0.17ST ceramics were prepared via a solid-state reaction method by using high-purity (>99%) $Na_2CO_3$, $Nb_2O_5$, $SrCO_3$, and $TiO_2$ as raw materials. The powders were mixed thoroughly in ethanol using zirconia balls for 10 h according to their compositional formula. The mixture was ball-milled again for 10 h after calcination at 900 °C for 5 h. The sample compacts were densified by a two-step sintering. The samples were first heated at 5 °C/min to $T_1$, then cooled at 10 °C/min to $T_2$ and held at $T_2$ for 2–4 h, as shown in Table 1.

The crystal structure was examined by an X-ray diffractometer (XRD, D/Max-RB, Rigaku, Tokyo, Japan) using Cu K$\alpha$ radiation. To quantitatively describe the phase structure, we analyzed the XRD data by the Rietveld refinement using GSAS software. The microstructure

**Table 1. Sintering Parameters, Relative Densities and Average Grain Sizes of 0.83NN-0.17ST Ceramics Achieved by Two-Step Sintering**

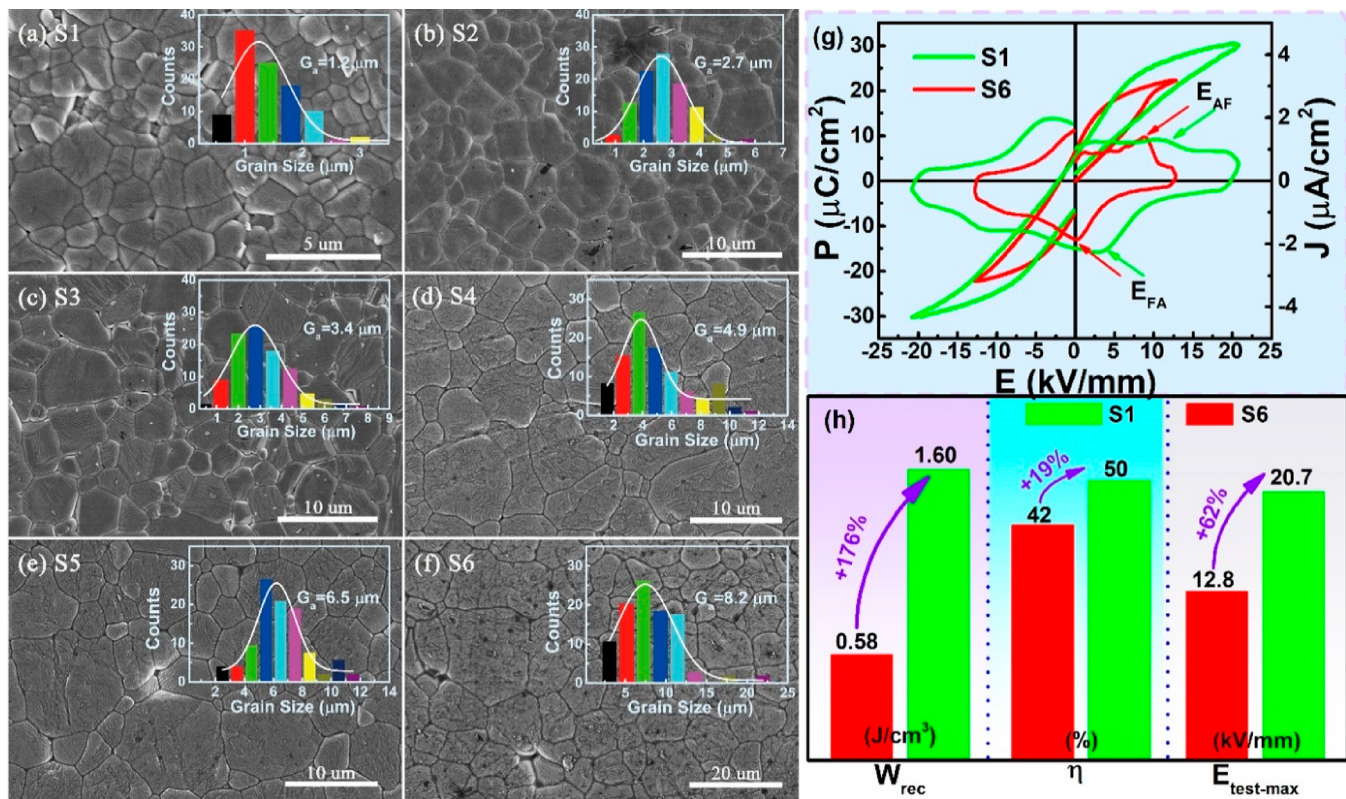| sintering temperature ($T_1/T_2$) (°C) | holding time (h) | relative density (%) | average grain size ($\mu$m) | sample no. |
|---|---|---|---|---|
| 1350/1280 | 2 | 95 | 1.2 | S1 |
| 1350/1280 | 4 | 96 | 2.7 | S2 |
| 1350/1300 | 2 | 96 | 3.4 | S3 |
| 1350/1300 | 4 | 97 | 4.9 | S4 |
| 1400/1300 | 2 | 98 | 6.5 | S5 |
| 1400/1300 | 4 | 98 | 8.2 | S6 |

**Figure 2.** (a−f) SEM images on the polished and thermally etched surfaces of 0.83NN-0.17ST ceramics by two-step sintering. Samples are numbered as S1−S6 in the sequence of the increase of the average grain size ($G_a$). (g) $P$−$E$ loops and the corresponding $J$−$E$ curves for S1 and S6 samples measured under their maximum testable electric fields at 10 Hz; (h) a comparison of $W_{rec}$, and $E_{test-max}$ between S1 and S6 samples.
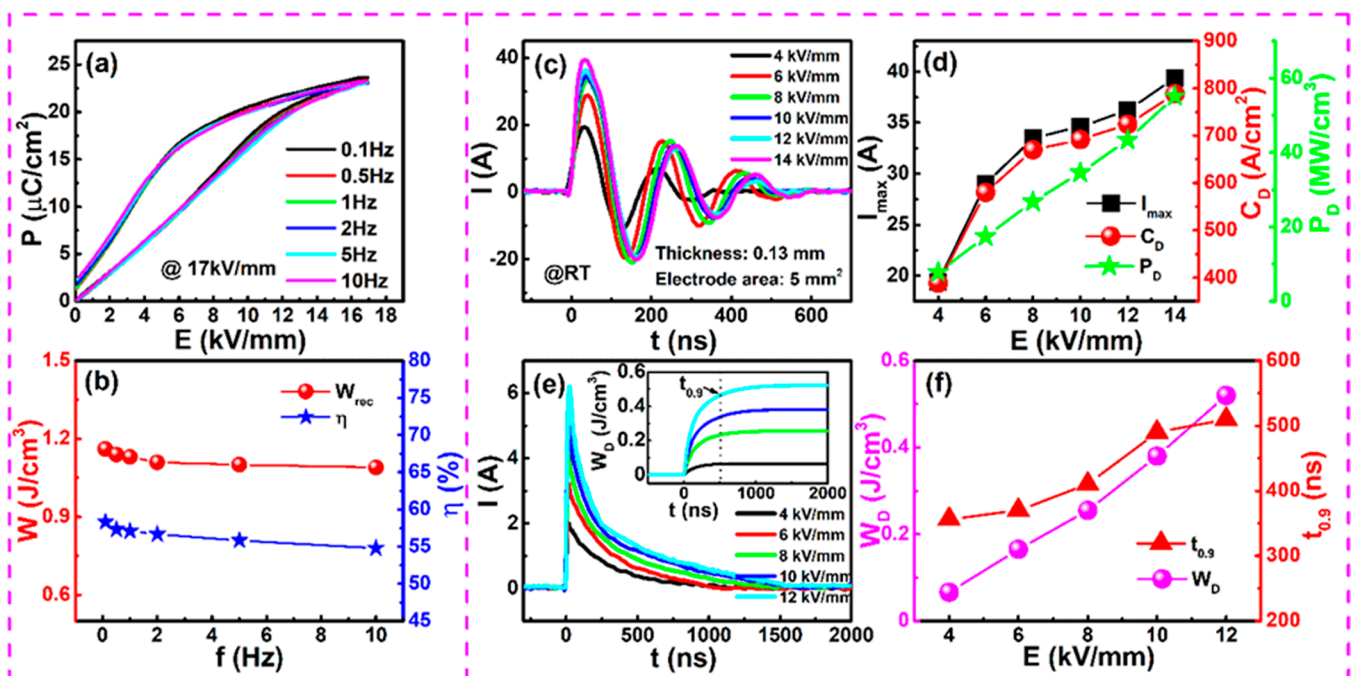


**Figure 3.** (a) $P$−$E$ loops of the S1 sample measured at room temperature in the frequency range of 0.1−10 Hz; (b) $W_{rec}$ and $\eta$ values as a function of frequency; (c) room-temperature pulsed underdamped discharging current curves of the S1 sample under various electric fields; (d) variation in $I_{max}$, $C_D$, and $P_D$ with the applied electric field; (e) room-temperature pulsed overdamped discharging current curves of the S1 sample at a fixed load resistance of 300 Ω under various electric fields; and (f) $W_D$ and $t_{0.9}$ values as a function of the applied electric field for the S1 sample. The inset of e shows the $W_D$−$t$ curves under different electric fields.

of the ceramic specimens was observed by a field-emission scanning electron microscope (FE-SEM, SU8020, JEOL, Tokyo, Japan). Before

the SEM observation, the samples were polished and thermally etched at ~1150 °C for 20 min. The dielectric properties at various

temperatures and frequencies were measured using a broad frequency dielectric spectrometer (Concept 80, Novocontrol Inc., Germany) at a heating rate of 3 °C/min. Impedance spectroscopy was measured using a precise impedance analyzer (4294A, Agilent Technologies, Santa Clara, CA, USA). The $E_B$ measurement was performed at room temperature by using a voltage-withstand test device (BDJC-50KV, Beiguangjingyi Instrument Equipment Co. Ltd., Beijing, China). Raman spectra were collected on well-polished samples by 532 nm laser excitation using a Raman spectrometer (LabRam HR Evolution, HORIBA JOBIN YVON, Longjumeau Cedex, France). The $P-E$ hysteresis loops were measured by using an FE measuring system (Precision multiferroelectric, Radiant Technologies Inc., Albuquerque, NM) and the sample size is 0.13 mm (thickness) $\times$ 5 mm$^2$ (electrode area). The energy release characteristics of ceramic capacitors were investigated by a charge−discharge platform (CFD-001, Gogo Instruments Technology, Shanghai, China) with a certain discharge resistance, inductance, and capacitance load circuit (RLC).

## 3. RESULTS AND DISCUSSION

The SEM micrographs of the as-sintered 0.83NN-0.17ST ceramic samples are presented in Figure 2a−f. Samples are numbered as S1−S6 according to the increase of grain size, which were achieved by varying two-step sintering parameters. It can be seen from Figure 2 and Table 1 that all samples have been well densified with a high relative density of ≥95%, indicating little influence of the sample density on the AFE phase stability.[48] The grain size distribution of different ceramic samples were analyzed according to the fitting by *Gauss* function, as shown in the insets of Figure 2a−f and Table 1. The change in sintering parameters has resulted in the preparation of well-densified ceramic samples having a wide average grain size range from ~1.2 to ~8.2 $\mu$m. The suppression of grain growth was mainly ascribed to the lack of grain boundary migration but the validity of grain boundary diffusion or bulk diffusion through selecting appropriate holding temperatures ($T_2$) during two-step sintering.[49]

Figure 2g shows the $P-E$ loops and the corresponding polarization current density-electric field ($J-E$) curves for S1 and S6 samples with smallest and largest average grain size under their maximum testable electric fields ($E_{test-max}$), respectively. An obviously slim $P-E$ loop can be obtained on both samples, but the S1 sample have a much larger $E_{test-max}$ than the S6 sample (Figure 2h, increase by ~62%), meaning that the former with smaller grain size probably owns a larger $E_B$ value. As indicated in Figure 2h, the $W_{rec}$ value of the fine-grain S1 sample can be increased by 176% as compared with that of the coarse-grain S6 sample, which approximates to 1.60 J cm$^{-3}$ and 0.58 J cm$^{-3}$, respectively. At the same, the $\eta$ value was enhanced by 19%.

Furthermore, $P-E$ loops measured under different frequencies for the S1 ceramic are further shown in Figure 3a. It can be seen that $P-E$ loops exhibit a weak frequency dependence in the measured frequency range. The AFE-FE phase transition and the domain wall motion lag as the measurement frequency increases, leading to an increase in $E_{AF}$ but a decrease in $E_{FA}$. A small reduction in $P_{max}$ with increasing frequency mainly comes from the time effect of field induced FE polarization response as the applied electric field is larger than $E_{AF}$. As a result, both $W_{rec}$ and $\eta$ values decrease slightly from ~1.16 J/cm$^3$ and ~58 to ~1.09 J/cm$^3$ and ~55% with increasing frequency from 0.1 to 10 Hz, respectively, as shown in Figure 3b.

Pulsed charging−discharging measurement was used to evaluate the actual energy-storage performance of the ceramic capacitor. Figure 3c illustrates the electric-field-dependent

underdamped pulsed discharge electric current−time ($I-t$) curves for the S1 ceramic at room temperature. The stored charge was found to be released rapidly (≤600 ns) under different electric fields. The variation of the first current peak amplitude ($I_{max}$), current density ($C_D = I_{max}/S$) and power density ($P_D = EI_{max}/2S$; $S$ denotes the electrode area of the sample and $E$ is the electric field strength) as a function of the applied electric field can be obtained from the $I-t$ curves of the S1 ceramic, as shown in Figure 3d. The value of $I_{max}$ increases from 19.5 A at 4 kV/mm to 40 A at 14 kV/mm. Moreover, the corresponding $C_D$ and $P_D$ at 14 kV/mm reach their maximum values of 788 A/cm$^2$ and 55 MW/cm$^3$, respectively. The high values of $C_D$ and $P_D$ indicate that the S1 sample is superior to some other reported dielectric ceramics,[18,19,50−52] as compared in Table 2, hopefully becoming potential candidates for the application in pulsed power capacitors.

**Table 2. Comparison of Charge−Discharge Properties between the S1 Sample and Some Other Promising Energy-Storage Dielectric Ceramics**

| composition | $E$ (kV/mm) | $C_D$ (A/cm$^2$) | $P_D$ (MW/cm$^3$) | $t_{0.9}$ (ns) | ref |
|---|---|---|---|---|---|
| PLZST | 4 | 447 | 8.94 | | 50 |
| PLBZST | 6.67 | 242 | 8 | ~1000 | 51 |
| BT-BNZ | 6 | | 6.15 | ~1706 | 52 |
| NN-BMNN | 10 | 382 | 19 | | 18 |
| NN-BZT | 12 | 642 | 38 | ~50 | 19 |
| This work | 14 | 788 | 55 | ~500 | |

$^a$The following abbreviations are used: PLZST, Pb$_{0.94}$La$_{0.04}$(Zr$_{0.4704}$Sn$_{0.3696}$Ti$_{0.16}$)O$_3$; PLBZST, Pb$_{0.90}$La$_{0.04}$Ba$_{0.04}$[(Zr$_{0.7}$Sn$_{0.3}$)$_{0.88}$Ti$_{0.12}$]O$_3$; BT-BNZ, 0.90BaTiO$_3$-0.10 Bi(Zn$_{0.5}$Zr$_{0.5}$)O$_3$; NN-BMNN, 0.85NaNbO$_3$-0.15 Bi(Mg$_{2/3}$Nb$_{1/3}$)-NbO$_3$; NN-BZT, 0.91NaNbO$_3$-0.09 Bi(Zn$_{0.5}$Ti$_{0.5}$)O$_3$.

Overdamped discharge curves as a function of electric field are shown in Figure 3e. According to the overdamped discharge curves, the discharge energy density under different electric fields ($W_D = R \int I(t)^2 dt/V$, where $V$ is the sample volume and $R$ is the total load resistor of 300 $\Omega$) can be obtained, as shown in the inset of Figure 3e. The current peak ($I_{max}$) and $W_D$ values increase with increasing electric field, from 2 A and 0.07 J/cm$^3$ at 4 kV/mm to 6.2 A and 0.52 J/cm$^3$ at 12 kV/mm, respectively. The discharge rate can be estimated by discharge time ($t_{0.9}$), which describes the time just corresponding to reaching 90% saturated $W_D$ value. Under a relatively low electric field of ~4 kV/mm, the S1 ceramic sample shows a fast discharge rate with a short $t_{0.9} \approx 350$ ns owing to little contribution from the AFE-FE phase transition. $t_{0.9}$ increases with increasing electric field because of a gradual increase of the contribution of the AFE domain reorientation and the AFE-FE phase transition, both of which show much slower response to external electric field than the domain wall vibration/motion in the lower electric field range than $E_{AF}$. Nevertheless, a short $t_{0.9}$ of <520 ns can be found for the S1 sample in the studied electric field range.

Although the significant improvement of energy-storage properties from S6 to S1 samples seems to be ascribed to the obviously enhanced applicable electric field magnitudes (Figure 2h), the fundamental physical mechanism still needs to be clarified by means of multiscale characterization. Figure 4a,b show $P-E$ hysteresis loops and the corresponding $J-E$ curves of 0.83NN-0.17ST ceramics under the same electric
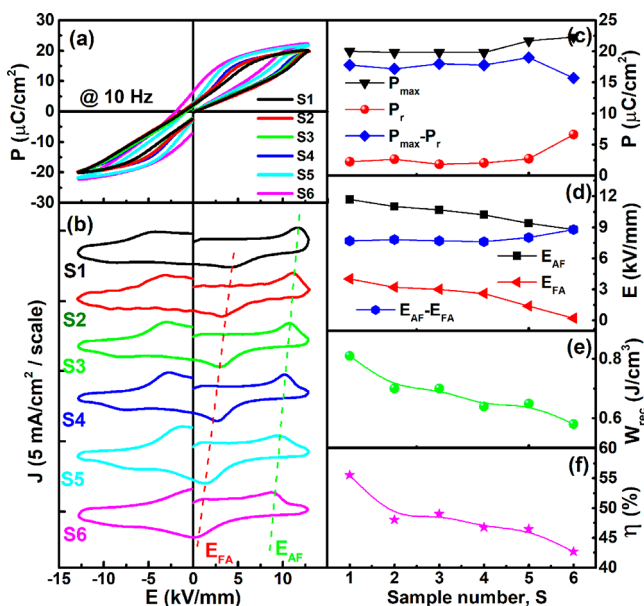
**Figure 4.** (a) $P-E$ hysteresis loops and (b) the corresponding $J-E$ curves for 0.83NN-0.17ST ceramics with different grain sizes at room temperature. The evolution of (c) $P_{max}$, $P_r$, and $P_{max}-P_r$; (d) $E_{AF}$, $E_{FA}$ and $E_{AF}-E_{FA}$; (e) $W_{rec}$; and (f) $\eta$ values of different samples from S1 to S6.

field. Double-like $P-E$ loops as well as double current peaks can be observed in all the studied samples, indicating typical AFE behavior. The evolution of $P_{max}$, $P_r$, $P_{max}-P_r$, $E_{AF}$, $E_{FA}$, and $E_{AF}-E_{FA}$ with changing grain size is shown Figure 4c, d. Both $P_{max}$ and $P_r$ decrease slightly with decreasing average grain size, because of the increased pinning effect of grain boundary on domain switching and the reduced phase switching hysteresis for stabilized AFE phases,[26,27] respectively. A large $P_{max}-P_r$ value of over 15 $\mu C/cm^2$ can be obtained in the studied ceramic samples. As grain size decreases, both $E_{AF}$ and $E_{FA}$ values increase, probably because of the decrease and increase in the effective electric field on grains and grain boundaries, respectively. The increase in grain boundary content would lead to the increase of grain boundary resistance which causes the grain boundaries to share more electric fields. Large $P_{max}-P_r$ and increased $E_{AF}$ are responsible for the enhanced $W_{rec}$ of the 0.83NN-0.17ST samples with decreasing grain size, as shown in Figure 4e. Most importantly, it can be seen that the difference value between $E_{AF}$ and $E_{FA}$ ($E_{AF}-E_{FA}$), which is an important parameter to evaluate the hysteresis of the AFE-FE phase transition, decreases slightly with decreasing grain size, thus leading to the enhancement of the energy-storage efficiency $\eta$, as shown in Figure 4f. This may be ascribed to the increase of internal stress between grains as grain size decreases.[27,53] Nevertheless, grain size engineered AFE ceramics were found to achieve largely tunable energy-storage properties through changing AFE-FE and FE-AFE phase transition, and AFE and FE domain switching process based on typical boundary effects.

Figure 5a,b show permittivity versus temperature and frequency curves and Raman spectra of S1−S6 ceramic samples, respectively. It can be found that the dielectric relaxation degree obviously increases from S6 to S1 samples, as characterized by the increase of the relaxation factor $\Delta T_{relax}$ ($=T_{m,1\ MHz}-T_{m,1\ kHz}$) and the diffuseness degree $\gamma$, and the decrease of the temperature at the maximum dielectric

permittivity ($T_m$) (see the inset of Figure 5a). The appearance of dielectric relaxor behavior is usually related to the enhanced random (electric or strain) fields due to the local composition disorder,[54,55] as characterized by Raman spectra shown in Figure 5b. The coarse-grain S6 sample exhibits obviously split multipeaks in the wavenumber range of 100−300 cm$^{-1}$, which mainly correspond to the bending modes of the NbO$_6$ octahedra as a result of the antiparallel off-centering displacement of B-site cations. By comparison, the Raman peaks become obviously broadening and blurry from S6 to S1 samples, thus leading to a nearly smooth Raman spectrum for the S1 sample. According to the deconvolution results, little change in the number of Raman peaks suggests the unchanged local symmetry. However, evidently increased full width at half-maximum (fwhm) and decreased peak intensity for both $\nu_5$ and $\nu_1$ vibration modes suggest the increase of structural disorder and the decrease of the unit cell polarity, as shown in Figure 5c, d where the intensity and fwhm for typical $\nu_5$ and the $\nu_1$ modes are mainly related to the vibration of the B−O bond and the BO$_6$ octahedra tilting configuration, respectively. The formation of the local heterogeneity might be related to insufficient mass transfer as a result of little holding time at high-temperature $T_1$ during two-step sintering. The resulting local random fields would influence the phase switching between AFE and FE in response to external electric fields. In comparison with normal AFEs, the existence of larger local random fields in relaxor AFEs can effectively impede the growth of nanodomains and the subsequent phase transition process,[7] leading to higher $E_{AF}$. Simultaneously, the larger local random fields also provide a restoring force, which makes the back-switching process of FE to AFE easier, producing higher $E_{FA}$ and lower hysteresis as well, as shown in Figure 4d.

As known, impedance spectroscopy is a powerful tool to investigate electrical conduction and dielectric relaxation mechanism. Figure 6a shows the $Z'-Z''$ curves for S1−S6 samples measured at 425 °C in the frequency range of 20 Hz to 1 MHz. $Z'$ and $Z''$ are the real and imaginary parts of impedance, respectively. It can be seen that all of the studied samples exhibit a nearly single impedance arc. However, these arcs are unable to be fitted by an RC equivalent circuit, indicating the existence of contributions from both grains and grain boundaries.[56] In order to distinguish the respective contribution of grains and grain boundaries, it is necessary to construct an equivalent analog circuit for fitting, as shown in the inset of Figure 6a. This circuit is composed of a series of grain and grain boundary components, including grain resistance ($R_g$), grain capacitance ($C_g$), grain boundary resistance ($R_{gb}$), and grain boundary capacitance ($C_{gb}$). A good agreement between the fitted lines and the tested results indicates that the adopted fitting circuit is equivalent to the experimental results. Figure 6b shows the quantitative relationship between grain resistivity ($\rho_g$), grain boundary resistivity ($\rho_{gb}$) and total resistivity ($\rho_{total}$) of each sample at 425 °C. It can be found that the main contribution to the macroscopic resistivity comes from grain boundary for each sample. $\rho_{gb}$ obviously increases with decreasing grain size from S6 to S1 due to the increased fraction of grain boundary.[56,57] The slightly increased $\rho_g$ with decreasing grain size should be ascribed to the decrease of oxygen vacancies and defects probably as a result of the reduction of the volatilization of sodium caused by improved sintering processes. Figure 6c shows the $Z''/Z''_{max}$ as a function of frequency for the S1 ceramic in the temperature range of 400−500 °C. Only one
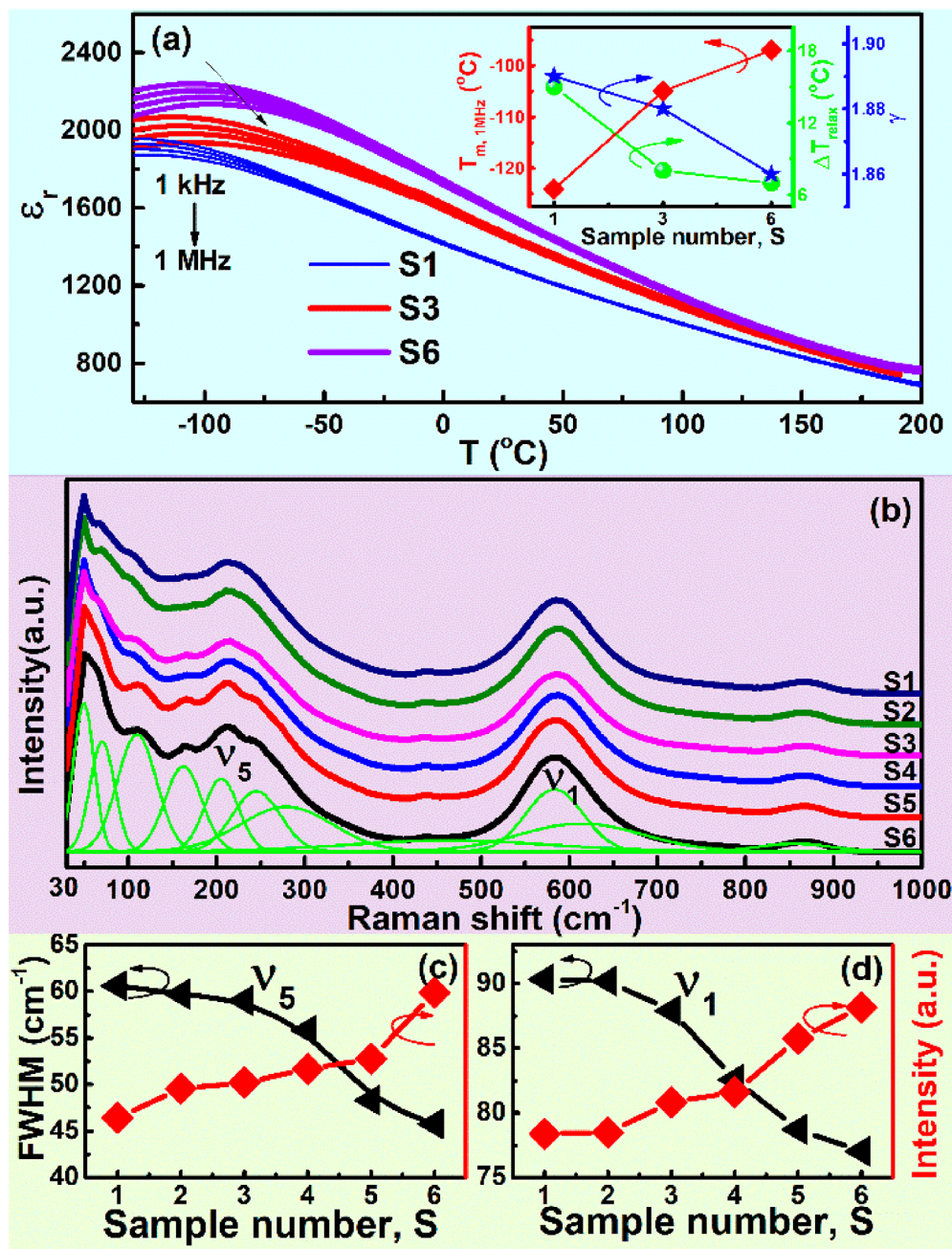
**Figure 5.** (a) Dielectric permittivity of S1, S3, and S6 samples as a function of temperature and frequency measured on heating; (b) room-temperature Raman spectra of S1−S6 samples; variation in peak intensity and fwhm of (c) $\nu_5$ and (d) $\nu_1$ Raman vibration modes. The inset of a shows the values of $\Delta T_{relax}$, $\gamma$, and $T_m$ as a function of sample number.

peak can be observed, which shifts toward higher frequency with increasing temperature, indicating that the temperature-dependent relaxation behavior is mainly caused by defects or vacancies in the ceramic. Moreover, the activation energy of the conductivity can be calculated by the Arrhenius equation:[58]

$$\sigma = \sigma_0 \exp(E_a/kT) \quad (1)$$

where $\sigma$ (= $1/\rho$, where $\rho$ is resistivity) is the bulk conductivity, $\sigma_0$ is the pre-exponent constant, $E_a$ is the activation energy of conduction, and $k$ is the Boltzmann constant. $E_a$ can be calculated from the slope of $\ln \sigma - 1000/T$ plots, as shown in the inset of Figure 6d using the linear fitting results of the S1 ceramic as an example. It has been reported that the activation energies of single ionized oxygen vacancies and double ionized

oxygen vacancies are in the range of 0.3−0.5 eV and 0.6−2 eV,[59,60] respectively. The activation energies of grain and grain boundary are both in the range of 0.67−1.76 eV for S1−S6 ceramics, as shown in Figure 6d, demonstrating that they are mainly caused by double ionized oxygen vacancies. Moreover, $E_a$ values for both grain and grain boundary increase with decreasing grain size, bringing about higher potential barriers for the diffusion of oxygen vacancies. The enhanced resistivity and the increased steadiness of oxygen vacancies with decreasing grain size should be also beneficial for the improved $E_B$.

The $E_B$ value can be experimentally evaluated through the Weibull distribution using the following equations:[61]
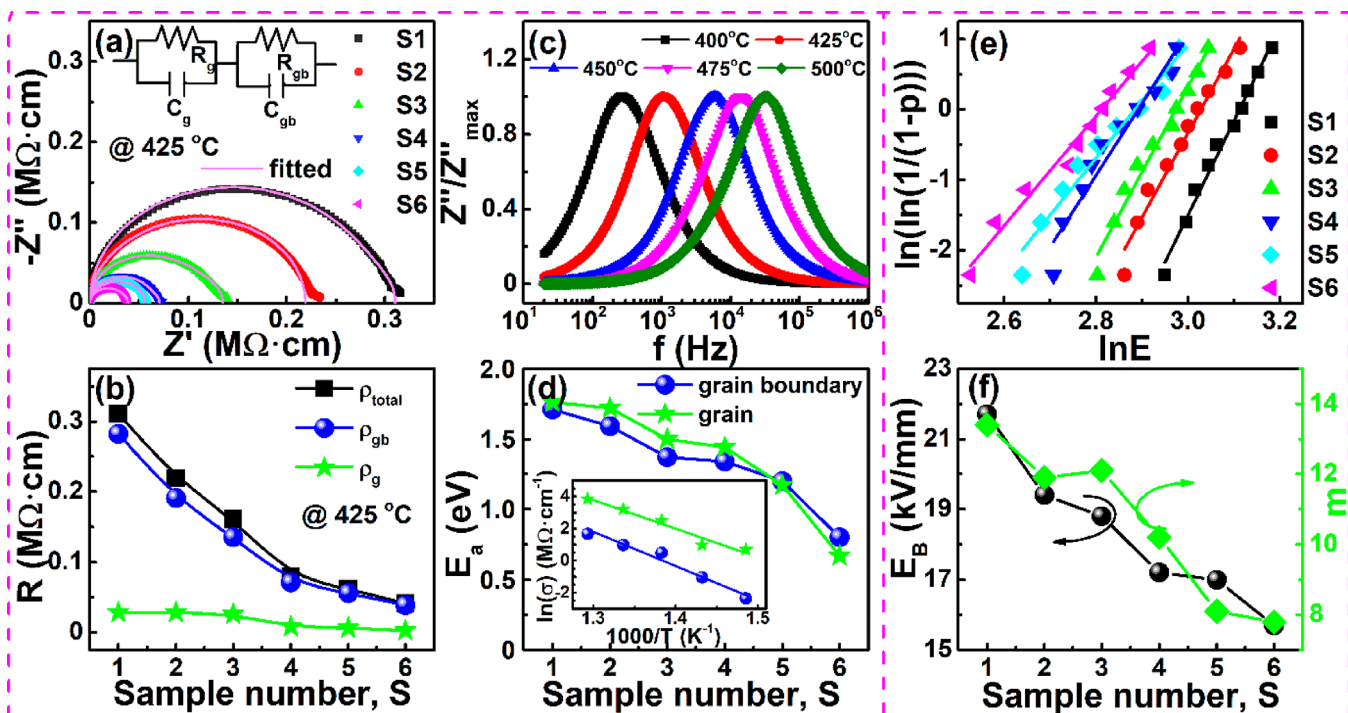
**Figure 6.** (a) Complex AC impedance and fitting semicircles at 425 °C for the S1−S6 samples, (b) the values of $\rho_{total}$, $\rho_g$, and $\rho_{gb}$ obtained from the fitting results, (c) plots of $Z''/Z''_{max}$ versus frequency in the temperature range of 400−500 °C for the S1 ceramic, (d) the variation in the activation energy ($E_a$) of grain and grain boundary conductivity for the S1−S6 ceramics. The inset of (d) is the Arrhenius-type plots of bulk conductivity of the grain and grain boundary for the S1 ceramic. (e) Weibull distributions and fitting lines of the breakdown strength $E_B$, and the determined $E_B$ and the Weibull modulus $m$ of the S1−S6 ceramics.

$$X_i = \ln(E_i) \tag{2}$$

$$Y_i = \ln\{\ln[1/(1 - i/n + 1)]\} \tag{3}$$

where $n$ is the sum of all samples, $E_i$ is the breakdown electric field for each sample, and $i$ is the serial number of samples. The samples are arranged in ascending order so that $E_1 \leq E_2 \leq ... E_i ... \leq E_n$. The value of $E_B$ can be evaluated by the Weibull distribution through a linear fitting between $X_i$ and $Y_i$. The slope of the line (shape parameter $m$) is related to the range of the $E_B$, whereas the intercept on the $x$-axis is related to the magnitude of the $E_B$. The fitting results are displayed in Figure 6e, f. The shape parameter $m$ of all compositions is larger than 7, proving high reliability of the obtained $E_B$ values. It is obvious that all data fit well with the Weibull distribution with good linear relationship between $X_i$ and $Y_i$. It can be found that the average $E_B$ increases monotonously with decreasing grain size in the studied grain size range. As a result, the $E_B$ value usually has an exponential decay relationship with average grain size ($G_a$), i.e., $E_B \propto (G_a)^{-a}$ on the basis of high relative density.[28] Actually, because of the increased local composition disorder, the vague polarization current peak caused by sluggish switching process should also help improve the dielectric breakdown behavior.

## 4. CONCLUSIONS

Recoverable energy-storage density can be remarkably amplified in two-step sintered 0.83NN-0.17ST lead-free relaxor AFE R-phase ceramics by means of dual adjustment of local heterogeneity and grain scale. Obviously enhanced dielectric relaxation behavior and significantly refined grain morphology synergetically contribute to energy-storage properties from different structure scales through optimizing the phase switching process between AFE and FE phases and increasing the effective dielectric breakdown strength $E_B$. As a result, the S1 sample with average grain size ~1.2 $\mu$m has a $W_{rec}$ of ~1.60 J/cm^{3}, which is about 2.76 times of the $W_{rec}$ value for the S6 sample with average grain size ~8.2 $\mu$m. Moreover, the fine-grain S1 sample also exhibits a fast discharge time (≤520 ns), large current density (788 A/cm^{2}), and large power density (55 MW/cm^{3}), illustrating great potentials for high-power pulsed capacitor applications.

## ■ AUTHOR INFORMATION

### Corresponding Author

**Ruzhong Zuo** − Institute of Electro Ceramics & Devices, School of Materials Science and Engineering, Hefei University of Technology, Hefei 230009, China; ⊙ orcid.org/0000-0001-8295-4323; Email: piezolab@hfut.edu.cn

### Authors

**Aiwen Xie** − Institute of Electro Ceramics & Devices, School of Materials Science and Engineering, Hefei University of Technology, Hefei 230009, China

**He Qi** − Institute of Electro Ceramics & Devices, School of Materials Science and Engineering, Hefei University of Technology, Hefei 230009, China; ⊙ orcid.org/0000-0002-3094-3574

Complete contact information is available at:
https://pubs.acs.org/10.1021/acsami.0c00831

### Notes

The authors declare no competing financial interest.

### ■ REFERENCES

(1) Chauhan, A.; Patel, S.; Vaish, R.; Bowen, C. R. Anti-Ferroelectric Ceramics for High Energy Density Capacitors. *Materials* **2015**, *8*, 8009−8031.

(2) Liu, Z.; Lu, T.; Ye, J. M.; Wang, G. S.; Dong, X. L.; Withers, R.; Liu, Y. Antiferroelectrics for Energy Storage Applications: A Review. *Adv. Mater. Technol.* **2018**, *3*, 1800111.

(3) Yang, L.; Kong, X.; Li, F.; Hao, H.; Cheng, Z.; Liu, H.; Li, J.-F.; Zhang, S. Perovskite Lead-Free Dielectrics for Energy Storage Applications. *Prog. Mater. Sci.* **2019**, *102*, 72−108.

(4) Hao, X. H.; Zhai, J. W.; Kong, L. B.; Xu, Z. K. A Comprehensive Review on the Progress of Lead Zirconate-Based Antiferroelectric Materials. *Prog. Mater. Sci.* **2014**, *63*, 1−57.

(5) Yao, Z. H.; Song, Z.; Hao, H.; Yu, Z. Y.; Cao, M. H.; Zhang, S. J.; Lanagan, M. T.; Liu, H. X. Homogeneous/Inhomogeneous-Structured Dielectrics and their Energy-Storage Performances. *Adv. Mater.* **2017**, *29*, 1601727.

(6) Zhao, L.; Liu, Q.; Gao, J.; Zhang, S. J.; Li, J. F. Lead-Free Antiferroelectric Silver Niobate Tantalate with High Energy Storage Performance. *Adv. Mater.* **2017**, *29*, 1701824.

(7) Qi, H.; Zuo, R. Z.; Xie, A. W.; Tian, A.; Fu, J.; Zhang, Y.; Zhang, S. J. Ultrahigh Energy-Storage Density in NaNbO$_3$-Based Lead-Free Relaxor Antiferroelectric Ceramics with Nanoscale Domains. *Adv. Funct. Mater.* **2019**, *29*, 1903877.

(8) Wang, H. S.; Liu, Y. C.; Yang, T. Q.; Zhang, S. J. Ultrahigh Energy-Storage Density in Antiferroelectric Ceramics with Field-Induced Multiphase Transitions. *Adv. Funct. Mater.* **2019**, *29*, 1807321.

(9) Liu, X. H.; Li, Y.; Hao, X. H. Ultra-High Energy-Storage Density and Fast Discharge Speed of $(Pb_{0.98-x}La_{0.02}Sr_x)(Zr_{0.9}Sn_{0.1})_{0.995}O_3$ Antiferroelectric Ceramics Prepared via the Tape-Casting Method. *J. Mater. Chem. A* **2019**, *7*, 11858−11866.

(10) Gao, P.; Liu, Z. H.; Zhang, N.; Wu, H.; Bokov, A. A.; Ren, W.; Ye, Z. G. New Antiferroelectric Perovskite System with Ultrahigh Energy-Storage Performance at Low Electric Field. *Chem. Mater.* **2019**, *31*, 979−990.

(11) Liu, P.; Fan, B. Y.; Yang, G.; Li, W. R.; Zhang, H. B.; Jiang, S. L. High Energy Density at High Temperature in PLZST Antiferroelectric Ceramics. *J. Mater. Chem. C* **2019**, *7*, 4587−4594.

(12) Tian, Y.; Jin, L.; Zhang, H.; Xu, Z.; Wei, X.; Politova, E. D.; Stefanovich, S. Y.; Tarakina, N. V.; Abrahams, I.; Yan, H. High Energy Density in Silver Niobate Ceramics. *J. Mater. Chem. A* **2016**, *4*, 17279−17287.

(13) Zhou, M. X.; Liang, R. H.; Zhou, Z. Y.; Dong, X. L. Superior Energy Storage Properties and Excellent Stability of Novel NaNbO$_3$-Based Lead-Free Ceramics with A-Site Vacancy Obtained via A Bi$_2$O$_3$ Substitution Strategy. *J. Mater. Chem. A* **2018**, *6*, 17896−17904.

(14) Yang, Z. T.; Du, H. L.; Jin, L.; Hu, Q. Y.; Wang, H.; Li, Y. F.; Wang, J. F.; Gao, F.; Qu, S. B. Realizing High Comprehensive Energy Storage Performance in Lead-Free Bulk Ceramics via Designing an Unmatched Temperature Range. *J. Mater. Chem. A* **2019**, *7*, 27256−27266.

(15) Luo, N. N.; Han, K.; Zhuo, F. P.; Xu, C.; Zhang, G. Z.; Liu, L. J.; Chen, X. Y.; Hu, C. Z.; Zhou, H. F.; Wei, Y. Z. Aliovalent A-site Engineered AgNbO$_3$ Lead-Free Antiferroelectric Ceramics toward Superior Energy Storage Density. *J. Mater. Chem. A* **2019**, *7*, 14118−14128.

(16) Qi, H.; Zuo, R. Z. Linear-Like Lead-Free Relaxor Antiferroelectric $(Bi_{0.5}Na_{0.5})TiO_3$-NaNbO$_3$ with Giant Energy-Storage Density/Efficiency and Super Stability against Temperature and Frequency. *J. Mater. Chem. A* **2019**, *7*, 3971−3978.

(17) Xu, B.; Íñiguez, J.; Bellaiche, L. Designing Lead-Free Antiferroelectrics for Energy Storage. *Nat. Commun.* **2017**, *8*, 1−8.

(18) Ye, J. M.; Wang, G. S.; Zhou, M. X.; Liu, N. T.; Chen, X. F.; Li, S.; Cao, F.; Dong, X. L. Excellent Comprehensive Energy Storage Properties of Novel Lead-Free NaNbO$_3$-Based Ceramics for Dielectric Capacitor Applications. *J. Mater. Chem. C* **2019**, *7*, 5639−5645.

(19) Shi, R. K.; Pu, Y. P.; Wang, W.; Guo, X.; Li, J. W.; Yang, M. D.; Zhou, S. Y. A Novel Lead-Free NaNbO$_3$-Bi(Zn$_{0.5}$Ti$_{0.5}$)O$_3$ Ceramics System for Energy Storage Application with Excellent Stability. *J. Alloys Compd.* **2020**, *815*, 152356.

(20) Glazer, A. M.; Megaw, H. D. Studies of the Lattice Parameters and Domains in the Phase Transitions of NaNbO$_3$. *Acta Crystallogr., Sect. A: Cryst. Phys., Diffr., Theor. Gen. Crystallogr.* **1973**, *29*, 489−495.

(21) Zuo, R. Z.; Fu, J.; Qi, H. Stable Antiferroelectricity with Incompletely Reversible Phase Transition and Low Volume-Strain Contribution in BaZrO$_3$ and CaZrO$_3$ Substituted NaNbO$_3$ Ceramics. *Acta Mater.* **2018**, *161*, 352−359.

(22) Liu, Z. Y.; Lu, J. S.; Mao, Y. Q.; Ren, P. R.; Fan, H. Q. Energy Storage Properties of NaNbO$_3$-CaZrO$_3$ Ceramics with Coexistence of Ferroelectric and Antiferroelectric Phases. *J. Eur. Ceram. Soc.* **2018**, *38*, 4939−4945.

(23) Shimizu, H.; Guo, H. Z.; Reyes-Lillo, S. E.; Mizuno, Y.; Rabe, K. M.; Randall, C. A. Lead-Free Antiferroelectric: xCaZrO$_3$-(1-x)NaNbO$_3$ System ($0 \leq x \leq 0.10$). *Dalton Trans.* **2015**, *44*, 10763−10772.

(24) Chen, M.; Yao, X.; Zhang, L. Y. Grain Size Dependence of Dielectric and Field-Induced Strain Properties of Chemical Prepared (Pb, La)(Zr, Sn, Ti)O$_3$ Antiferroelectric Ceramics. *Ceram. Int.* **2002**, *28*, 201−207.

(25) Koruza, J.; Groszewicz, P.; Breitzke, H.; Buntkowsky, G.; Rojac, T.; Malic, B. Grain-Size-Induced Ferroelectricity in NaNbO$_3$. *Acta Mater.* **2017**, *126*, 77−85.

(26) Zhang, G. Z.; Liu, S. S.; Yu, Y.; Zeng, Y. K.; Zhang, Y. Y.; Hu, X.; Jiang, S. L. Microstructure and Electrical Properties of $(Pb_{0.87}Ba_{0.1}La_{0.02})(Zr_{0.68}Sn_{0.24}Ti_{0.08})O_3$ Anti-Ferroelectric Ceramics Fabricated by the Hot-Press Sintering Method. *J. Eur. Ceram. Soc.* **2013**, *33*, 113−121.

(27) Zhang, L.; Jiang, S. L.; Zeng, Y. K.; Fu, M.; Han, K.; Li, Q.; Wang, Q.; Zhang, G. Z. Y Doping and Grain Size Co-Effects on the Electrical Energy Storage Performance of $(Pb_{0.87}Ba_{0.1}La_{0.02})(Zr_{0.65}Sn_{0.3}Ti_{0.05})O_3$ Anti-Ferroelectric Ceramics. *Ceram. Int.* **2014**, *40*, 5455−5460.

(28) Tunkasiri, T.; Rujijanagul, G. Dielectric Strength of Fine Grained Barium Titanate Ceramics. *J. Mater. Sci. Lett.* **1996**, *15*, 1767−1769.

(29) Liu, B. B.; Wang, X. H.; Zhang, R. X.; Li, L. T. Grain Size Effect and Microstructure Influence on the Energy Storage Properties of Fine-Grained BaTiO$_3$-Based Ceramics. *J. Am. Ceram. Soc.* **2017**, *100*, 3599−3607.

(30) Waser, R. TrI4: The Role of Grain Boundaries in Conduction and Breakdown of Perovskite-Type Titanates. *Ferroelectrics* **1992**, *133*, 109−114.

(31) Jin, Q.; Pu, Y. P.; Wang, C.; Gao, Z. Y.; Zheng, H. Y. Enhanced Energy Storage Performance of Ba$_{0.4}$Sr$_{0.6}$TiO$_3$ Ceramics: Influence of Sintering Atmosphere. *Ceram. Int.* **2017**, *43*, S232−S238.

(32) Zhang, L.; Jiang, S. L.; Fan, B. Y.; Zhang, G. Z. Enhanced Energy Storage Performance in $(Pb_{0.858}Ba_{0.1}La_{0.02}Y_{0.008})$-$(Zr_{0.65}Sn_{0.3}Ti_{0.05})O_3$-$(Pb_{0.97}La_{0.02})(Zr_{0.9}Sn_{0.05}Ti_{0.05})O_3$ Anti-Ferroelectric Composite Ceramics by Spark Plasma Sintering. *J. Alloys Compd.* **2015**, *622*, 162−165.

(33) Huang, Y. H.; Wu, Y. J.; Qiu, W. J.; Li, J.; Chen, X. M. Enhanced Energy Storage Density of Ba$_{0.4}$Sr$_{0.6}$TiO$_3$-MgO Composite Prepared by Spark Plasma Sintering. *J. Eur. Ceram. Soc.* **2015**, *35*, 1469−1476.

(34) Song, Z.; Zhang, S. J.; Liu, H. X.; Hao, H.; Cao, M. H.; Li, Q.; Wang, Q.; Yao, Z. H.; Wang, Z. J.; Lanagan, M. T. Improved Energy Storage Properties Accompanied by Enhanced Interface Polarization in Annealed Microwave-Sintered BST. *J. Am. Ceram. Soc.* **2015**, *98*, 3212−3222.

(35) Pu, Y. P.; Zhang, L.; Cui, Y. F.; Chen, M. High Energy Storage Density and Optical Transparency of Microwave Sintered Homogeneous $(Na_{0.5}Bi_{0.5})_{(1-x)}Ba_xTi_{(1-y)}Sn_yO_3$ Ceramics. *ACS Sustainable Chem. Eng.* 2018, *6*, 6102−6109.

(36) Young, A.; Hilmas, G.; Zhang, S. C.; Schwartz, R. W. Effect of Liquid-Phase Sintering on the Breakdown Strength of Barium Titanate. *J. Am. Ceram. Soc.* 2007, *90*, 1504−1510.

(37) Zhang, Q. M.; Wang, L.; Luo, J.; Tang, Q.; Du, J. Improved Energy Storage Density in Barium Strontium Titanate by Addition of $BaO-SiO_2-B_2O_3$ Glass. *J. Am. Ceram. Soc.* 2009, *92*, 1871−1873.

(38) Yu, Z. L.; Liu, Y. F.; Shen, M.; Qian, H.; Li, F. F.; Lyu, Y. N. Enhanced Energy Storage Properties of $BiAlO_3$ Modified $Bi_{0.5}Na_{0.5}TiO_3-Bi_{0.5}K_{0.5}TiO_3$ Lead-Free Antiferroelectric Ceramics. *Ceram. Int.* 2017, *43*, 7653−7659.

(39) Zuo, R. Z.; Granzow, T.; Lupascu, D. C.; Rödel, J. PMN-PT Ceramics Prepared by Spark Plasma Sintering. *J. Am. Ceram. Soc.* 2007, *90*, 1101−1106.

(40) Adamczyk, M.; Kozielski, L.; Pawełczyk, M. Effect of Hot Pressing on Processing and Properties of BBN Ceramics. *Ceram. Int.* 2008, *34*, 1617−1622.

(41) Liu, X.; Xue, S. D.; Wang, F. F.; Zhai, J. W.; Shen, B. Grain Size Dependent Physical Properties in Lead-Free Multifunctional Piezoceramics: A Case Study of NBT-xST System. *Acta Mater.* 2019, *164*, 12−24.

(42) Kholkin, A.; Morozovska, A.; Kiselev, D.; Bdikin, I.; Rodriguez, B.; Wu, P. P.; Bokov, A.; Ye, Z. G.; Dkhil, B.; Chen, L. Q.; Kosec, M.; Kalinin, S. V. Surface Domain Structures and Mesoscopic Phase Transition in Relaxor Ferroelectrics. *Adv. Funct. Mater.* 2011, *21*, 1977−1987.

(43) Mohapatra, P.; Fan, Z. M.; Cui, J.; Tan, X. L. Relaxor Antiferroelectric Ceramics with Ultrahigh Efficiency for Energy Storage Applications. *J. Eur. Ceram. Soc.* 2019, *39*, 4735−4742.

(44) Shen, Z. B.; Wang, X. H.; Luo, B. C.; Li, L. T. $BaTiO_3-BiYbO_3$ Perovskite Materials for Energy Storage Application. *J. Mater. Chem. A* 2015, *3*, 18146−18153.

(45) Wu, J. Y.; Mahajan, A.; Riekehr, L.; Zhang, H. F.; Yang, B.; Meng, N.; Zhang, Z.; Yan, H. X. Perovskite $Sr_x(Bi_{1-x}Na_{0.97-x}Li_{0.03})_{0.5}TiO_3$ Ceramics with Polar Nano Regions for High Power Energy Storage. *Nano Energy* 2018, *50*, 723−732.

(46) Zhou, M. X.; Liang, R. H.; Zhou, Z. Y.; Yan, S. G.; Dong, X. L. Novel Sodium Niobate-Based Lead-Free Ceramics as New Environment-Friendly Energy Storage Materials with High Energy Density, High Power Density, and Excellent Stability. *ACS Sustainable Chem. Eng.* 2018, *6*, 12755−12765.

(47) Xie, A. W.; Qi, H.; Zuo, R. Z.; Tian, A.; Chen, J.; Zhang, S. J. An Environmentally-Benign $NaNbO_3$ Based Perovskite Antiferroelectric Alternative to Traditional Lead-Based Counterparts. *J. Mater. Chem. C* 2019, *7*, 15153−15161.

(48) Chao, L. M.; Hou, Y. D.; Zheng, M. P.; Zhu, M. K. High Dense Structure Boosts Stability of Antiferroelectric Phase of $NaNbO_3$ Polycrystalline Ceramics. *Appl. Phys. Lett.* 2016, *108*, 212902.

(49) Chen, I. W.; Wang, X. H. Sintering Dense Nanocrystalline Ceramics without Final-Stage Grain Growth. *Nature* 2000, *404*, 168−171.

(50) Xu, R.; Xu, Z.; Feng, Y. J.; Wei, X. Y.; Tian, J. J. Nonlinear Dielectric and Discharge Properties of $Pb_{0.94}La_{0.04}[(Zr_{0.56}Sn_{0.44})_{0.84}Ti_{0.16}]O_3$ Antiferroelectric Ceramics. *J. Appl. Phys.* 2016, *120*, 144102.

(51) Xu, R.; Xu, Z.; Feng, Y. J.; He, H. L.; Tian, J. J.; Huang, D. Temperature Dependence of Energy Storage in $Pb_{0.90}La_{0.04}Ba_{0.04}[(Zr_{0.7}Sn_{0.3})_{0.88}Ti_{0.12}]O_3$ Antiferroelectric Ceramics. *J. Am. Ceram. Soc.* 2016, *99*, 2984−2988.

(52) Yuan, Q. B.; Yao, F. Z.; Wang, Y. F.; Ma, R.; Wang, H. Relaxor Ferroelectric $0.9BaTiO_3-0.1 Bi(Zn_{0.5}Zr_{0.5})O_3$ Ceramic Capacitors with High Energy Density and Temperature Stable Energy Storage Properties. *J. Mater. Chem. C* 2017, *5*, 9552−9558.

(53) Xu, B. M.; Ye, Y. H.; Cross, L. E. Dielectric Properties and Field-Induced Phase Switching of Lead Zirconate Titanate Stannate Antiferroelectric Thick Films on Silicon Substrates. *J. Appl. Phys.* 2000, *87*, 2507−2515.

(54) Westphal, V.; Kleemann, W.; Glinchuk, M. D. Diffuse Phase Transitions and Random-Field-Induced Domain States of the "Relaxor" Ferroelectric $PbMg_{1/3}Nb_{2/3}O_3$. *Phys. Rev. Lett.* 1992, *68*, 847−850.

(55) Fisch, R. Random-Field Models for Relaxor Ferroelectric Behavior. *Phys. Rev. B: Condens. Matter Mater. Phys.* 2003, *67*, No. 094110.

(56) Badwal, S. P. S.; Drennan, J. Effect of Microstructure on Conductivity. *J. Mater. Sci.* 1987, *22*, 3231−3239.

(57) Gerstl, M.; Navickas, E.; Friedbacher, G.; Kubel, F.; Ahrens, M.; Fleig, J. The Separation of Grain and Grain Boundary Impedance in Thin Yttria Stabilized Zirconia (YSZ) Layers. *Solid State Ionics* 2011, *185*, 32−41.

(58) Laidler, K. J. The Development of the Arrhenius Equation. *J. Chem. Educ.* 1984, *61*, 494−498.

(59) Moos, R.; Hardtl, K. H. Electronic Transport Properties of $Sr_{1-x}La_xTiO_3$ Ceramics. *J. Appl. Phys.* 1996, *80*, 393−400.

(60) Pelaiz-Barranco, A.; Guerra, J. D. S.; Lopez-Noda, R.; Araujo, E. B. Ionized Oxygen Vacancy-Related Electrical Conductivity in $(Pb_{1-x}La_x)(Zr_{0.90}Ti_{0.10})_{1-x/4}O_3$ Ceramics. *J. Phys. D: Appl. Phys.* 2008, *41*, 215503.

(61) Weibull, W. A Statistical Distribution Function of Wide Applicability. *J. Appl. Mech.* 1951, *18*, 293−297.